RESEARCH ARTICLE

Adaptive RBF-FD method for contact problems

Jure Slak[1,2] | Gregor Kosec*[1]

[1]Parallel and Distributed Systems Laboratory, "Jožef Stefan" Institute, Slovenia

[2]Faculty of Mathematics and Physics, University of Ljubljana, Slovenia

Correspondence
*Gregor Kosec, Email: gregor.kosec@ijs.si

Present Address
Department E6
"Jožef Stefan" Institute
Jamova ulica 39
1000 Ljubljana
Slovenia

Summary

This paper proposes an original adaptive refinement framework, which combines the Radial Basis Functions-generated Finite Differences method and its prominent ability to tackle PDEs on scattered nodes without an exact mesh, with a simple nodal positioning algorithm that can distribute nodes according to an arbitrary density function. The framework is tested on three gradually more complex contact problems, governed by the Cauchy-Navier equations. First, a disk under pressure is considered and the computed stress field is compared to the closed form solution of the problem to assess the basic behaviour of the algorithm and the influence of free parameters. Second, a Hertzian contact problem, also with a known closed form solution, is studied to analyse the proposed algorithm with an ad-hoc error indicator and to test both refinement and derefinement. In the final case, a contact problem typical for fretting fatigue with no known closed form solution is considered and solved. It is demonstrated that the proposed methodology can be used in practical application and produces results comparable with FEM without the need for manual refinement or any human intervention.

KEYWORDS:
Linear elasticity, Radial Basis Functions, Adaptive h-refinement, Cauchy Navier equations, Contact problems, Meshfree methods

1 | INTRODUCTION

Solving partial differential equations (PDEs) with Radial basis functions (RBFs) began in 1990 when Kansa suggested that besides scattered data interpolation, RBFs could also be used for solving PDEs[1]. In the beginning only global collocation methods were used, achieving high order convergence and spectral accuracy[2], however at the cost of high computational complexity and possible ill-conditioning in solution of the global system, especially as the number of computational nodes increases. Shortcomings of the global methods encouraged the development of local approaches and soon several meshless methods based on approximation over local overlapping support domains appeared[3,4]. A popular variant among many local meshless methods is the Radial Basis Function-generated Finite Differences (RBF-FD) method, which uses finite difference-like collocation weights on an unstructured set of nodes[5]. The method has been successfully used in several problems and is still actively researched[6,7,8].

The most attractive feature of meshless methods is that they do not require an underlying mesh and fully define relations between nodes directly through their relative inter nodal positions, which allows to reduce the problem of constructing a mesh into a much simpler problem of positioning scattered nodes[9,10]. An obvious consequence is that meshless methods are able to locally modify node configurations by simply placing more points in areas where needed and removing them from areas that are overpopulated. A substantial amount of research has been done on adaptive meshless methods[11]. Meshless h-refinement, where

nodes are locally added or removed, has been successfully used with the global Radial Basis Function Collocation Method[12] in solution of nearly singular PDEs, as well as with local strong form meshless methods in solution of Burgers' equation[13] and torsion problem[14]. Meshless r-refinement, where the nodes are repositioned to improve the approximation with the total number of the nodes unchanged has been successfully used in solution of a phase field model[15]. Meshless adaptivity has also been used in crack propagation problems[16], and recently in finite volume method based meshless solution of an elasticity problem[17]. Even though the existence of easy refinement algorithms seems to be an inherent property of all meshless methods, one has to be careful when interfering with the nodal configuration to avoid potential negative effects such as ill conditioning and other possible complications[18,19] that arise with non smooth nodal distributions. This task becomes even more challenging in a fully automatic adaptivity setting, where the refinement algorithm has to be robust enough to fulfil the demands of the error indicator.

In the field of solid mechanics, where problems are traditionally tackled with the Finite Element Method (FEM)[20], meshless methods surfaced as a response to the cumbersome meshing of realistic 3D domains required by FEM[8,21,22,23]. The development began with weak form methods such as the Element Free Galerkin Method[24] and Meshless Local Petrov Galerkin Method[25], followed by strong form collocation approach that emerged with Finite Point Method (FPM)[26] and further developed with similar local strong form methods[8,22].

This paper continues the evolution of meshless methods in the field of linear elasticity by presenting a robust automatic refinement and derefinement algorithm coupled with RBF-FD discretisation technique. The algorithm relies on the node positioning algorithm that allows for node distributions conforming to an arbitrary density function. The performance of the method is demonstrated on three cases governed by Navier-Cauchy equations, gradually increasing in complexity. In the first case a disk under pressure is considered, which can be solved in closed form and is therefore ideal for testing, since the exact error can be computed during refinement. The second case considers Hertzian contact, where an ad-hoc error indicator based on the characteristics of the underlying problem, namely stress volatility, is used. The last case deals with numerical computation of stresses under fretting fatigue conditions, i.e. a contact with slip-stick zone that has been recently investigated with finite element analysis[27].

The rest of the paper is organized as follows: the refinement algorithm and all its components are described in Section 2, the results on three increasingly difficult cases are presented in Section 3 and finally, the conclusions are presented in Section 4.

2 | METHOD DESCRIPTION

Adaptive refinement of domain discretisations is indispensable in problems where varying precision and resolution of the numerical solution are required in different areas of the computational domain. A typical example of such problem in linear elasticity is a contact of two bodies where extremely high stress concentrations are present under and around the contact area. Solving such problems on uniform grids is completely intractable due to the amount of time and computational resources required. To obtain a numerical solution with satisfactory precision in the contact area within a reasonable time frame, many more nodes have to be placed under the contact than elsewhere. Since the areas of high stresses are generally not known a priori, and to eliminate the need for human intervention in construction of discretisations, a commonly adopted approach to such situations is to refine the discretisation iteratively, gradually increasing the resolution of the numerical solution in areas of interest. An error indicator is employed to identify the areas of interest with the ultimate goal to ensure relatively uniform error distribution throughout the domain or in many cases solely to solve the problem.

In this paper we combine the RBF-FD method, with its prominent ability to tackle PDEs on scattered nodes without an exact mesh, with a simple nodal positioning algorithm into an original adaptive refinement framework. The concept of the adaptively refined solution of a PDE in this work is as follows: initially discretise the domain with (usually) uniform nodal distribution, compute approximate solution u, compute new desired nodal density function based on input from the chosen error indicator, redistribute nodes and repeat as long as the error is not within desired range. This procedure is summarized as Algorithm 1.

In the following subsections all components of the solution procedure are described in the same order as they appear in Algorithm 1.

Algorithm 1 Adaptive solution procedure

Input: The problem, computation domain Ω, initial density function $\delta r : \Omega \rightarrow \mathbb{R}$ and the error threshold ε. **Output:** The numerical solution of the problem.

1: **function** ADAPTIVE_SOLVE(problem, Ω, δr, ε)
2:    $\mathcal{P} \leftarrow$ DISCRETISE(Ω, δr)   ▷ Discretises domain Ω as described in Section 2.1.
3:    solution $\leftarrow$ SOLVE(problem, $\mathcal{P}$)   ▷ Solves the problem using discretisation $\mathcal{P}$, see Section 2.2.
4:    error $\leftarrow$ ESTIMATE_ERROR(solution, $\mathcal{P}$)   ▷ Error indicator computation, see (26) or (29).
5:    **while** MEAN(error) $\geq \varepsilon$ **do**   ▷ Other error reductions such as MAX can be used.
6:       $\delta r \leftarrow$ ADAPT(δr)   ▷ Adapt the discretisation as described in Section 2.3.
7:       $\mathcal{P} \leftarrow$ DISCRETISE(Ω, δr)
8:       solution $\leftarrow$ SOLVE(problem, $\mathcal{P}$)
9:       error $\leftarrow$ ESTIMATE_ERROR(solution, $\mathcal{P}$)
10:   **end while**
11:   **return** solution
12: **end function**

2.1 | Filling nodes with variable density

Although mesh generation is not needed in RBF-FD, certain care still has to be taken to avoid too close node placements, which cause ill-conditioning. In other words, we seek the distribution of nodes that conforms to the treated domain shape and target nodal density, with the nodes also being distributed as regularly as possible.

The basis for the node placement procedure is the Poisson Disc Sampling algorithm[28]. The procedure begins with adding a starting "seed node" into the domain, followed by an iterative spreading of the populated area of the domain. In each iteration 6 new nodes are added regularly on a circle with centre in a randomly selected node p that has not been processed yet and radius $\delta r(p)$. The function δr is an external parameter and its value at point p represents the expected distance between neighbouring nodes around p, characterising the nodal density at that point. Some of these 6 nodes might be too close to the already positioned nodes, and thus a simple rejection criterion is used: if the distance to the closest node is closer than $\zeta \cdot \delta r(p)$, for $\zeta \in [0, 1]$, the node is removed. The proximity factor ζ must be used due to numerical errors in distance computations, however its use also produces smoother distributions. Is is typically set to 0.9 or 0.99. The algorithm is schematically presented in Fig. 1a.

After the domain is populated, the distribution is further regularised with an iterative algorithm that "diffuses" the nodes as if a repelling force was induced by theirs neighbours. The force is determined by summing the gradients of potentials in surrounding nodes, where the amplitude of the force is further normalised by the distance to the closest neighbour and δr. The algorithm also uses primitive "simulated annealing" techniques, i.e. the magnitude of translation is multiplied with an annealing factor that is linearly dropping from Q_i to Q_f. More precisely, in each node a repulsing force is computed as

$$d(i) = -\xi \left(\frac{N_r - n_r}{N_r}(Q_i - Q_f) + Q_i \right) \sum_{p_j \in \mathcal{N}(p_i)} \left(\frac{\delta r(p_j)}{\|p_j - p_i\|} \right)^\kappa (p_j - p), \tag{1}$$

where ξ stands for normalization factor, usually distance to the closest node, N_r represents the number of regularization iterations, n_r current iteration, Q_i initial "heat", Q_f final "heat", κ potential power and $\mathcal{N}(p)$ are neighbours of p. Typical set-up is $N_r \in [3, 10]$, $Q_i \in [0.8, 1.2]$, $Q_f \in [0, 0.2]$, $\kappa = 2$ and 3 closest neighbours are considered. The algorithm is schematically presented in Fig. 1b.

A simple demonstration of above algorithms is presented in Fig. 2. A scaled and shifted `peaks` function from Matlab was used as δr, specifically,

$$\delta r(x, y) = \delta x + (\Delta x - \delta x)(\text{peaks}(x, y) + 6.55)/14.66, \tag{2}$$

$$\text{peaks}(x, y) = 3(1 - x)^2 e^{-x^2 - (y+1)^2} - 10(x/5 - x^2 - y^5)e^{-x^2 - y^2} - \frac{1}{3}e^{-(x+1)^2 - y^2} \tag{3}$$

with $\delta x = 0.007$ and $\Delta x = 0.07$. A square region $[-3, 3] \times [-3, 3]$ was discretised, filled and regularised with described algorithms. The function δr is shown in Fig. 2a, and the initial and improved distributions are shown in Figures 2b and 2c, respectively. Additionally, zoomed-in versions are presented in Fig. 3 to better asses the node quality.
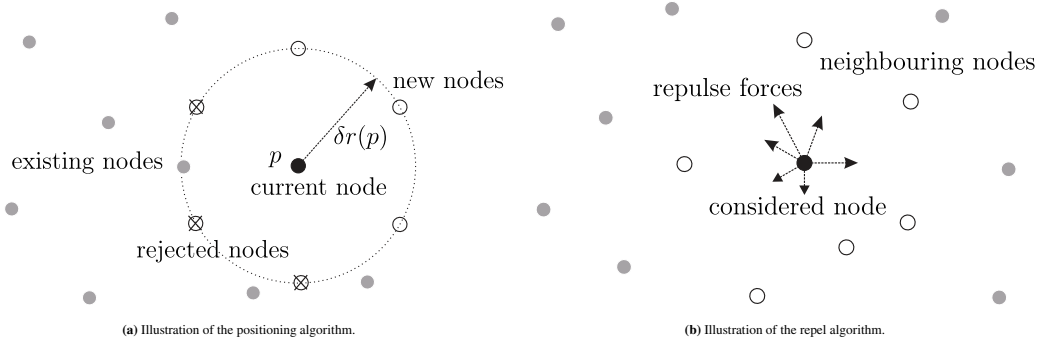
(a) Illustration of the positioning algorithm.

(b) Illustration of the repel algorithm.

FIGURE 1 Scheme of algorithms used for domain discretisation.

(a) Function δr.

(b) Nodes placed by the fill algorithm.

(c) Nodes after regularization.
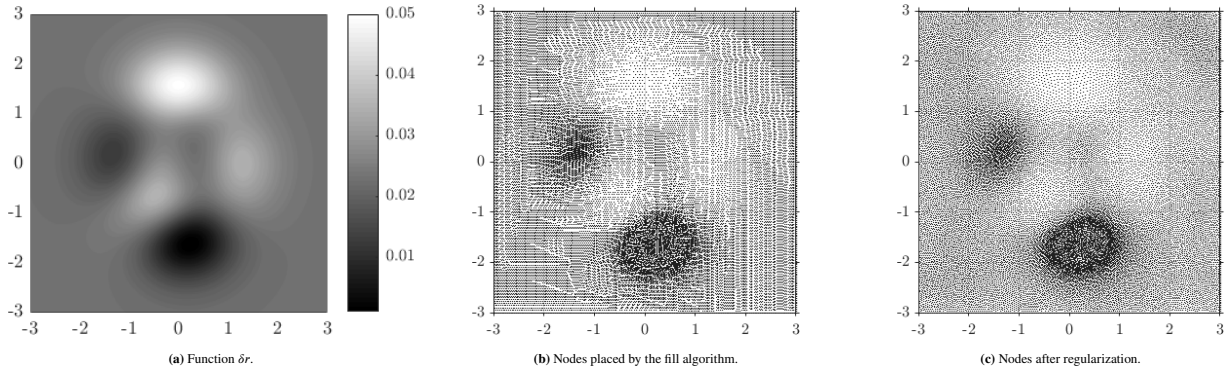
FIGURE 2 Illustration of domain discretisation with given function.

(a) Enlargement of Fig. 2a.

(b) Enlargement of Fig. 2b.

(c) Enlargement of Fig. 2c.
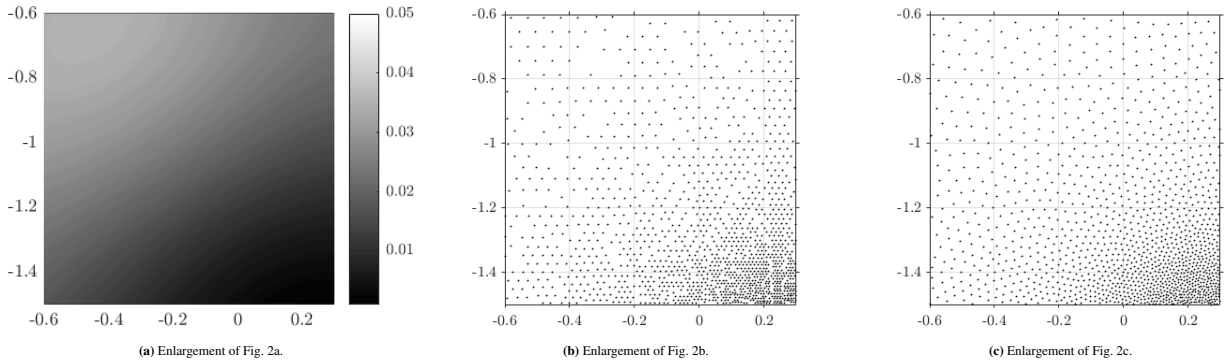
FIGURE 3 Enlarged versions of plots in Fig. 2.

Node generation is relatively undemanding from the computational point of view. The most expensive part of the fill algorithm is determining whether there are any proximity violations, which requires searching the closest nodes. However, this can be optimized with appropriate dynamic tree structures and managing the candidate list of possible nearby nodes. The regularization algorithm is a bit more expensive since it requires a full neighbourhood search in each iteration, but typically few iterations are needed to smooth out the irregularities.

2.2 | RBF-FD

The RBF-FD method is used to obtain the discrete formulation of a PDE. Consider an elliptic boundary value problem with Dirichlet boundary conditions

$$\mathcal{L}u = f \quad \text{on } \Omega \tag{4}$$

$$u = u_0 \quad \text{on } \partial\Omega, \tag{5}$$

where f and u_0 are known functions. To obtain a discrete representation, N nodes are placed in Ω, of which N_i nodes in the interior and N_b nodes on the boundary. Let the set of all discretisation nodes be denoted by $\mathcal{P}$. Each node p_i is assigned n_i neighbours (including itself), denoted $\mathcal{N}(p_i)$. These neighbours are commonly called the node's *support domain* or, analogous to the Finite Difference Method (FDM), its *stencil*.

The operator $\mathcal{L}$ is approximated as a weighted linear combination of function values at stencil points

$$(\mathcal{L}u)(p_i) \approx \sum_{p_j \in \mathcal{N}(p_i)} w_j^i u(p_j). \tag{6}$$

To determine the weights w_j^i, exactness of (6) is imposed for a certain set of functions. A common choice are monomials, as used in the FDM and FPM, however in RBF-FD method, as the name suggests, the Radial Basis Functions (RBFs) are used. RBFs, positioned in centres $P = \{p_1, \ldots, p_n\}$ are functions

$$\{\varphi_i := \varphi(\| \cdot - p_i\|), \text{ for } p_i \in P\}, \tag{7}$$

where $\varphi : [0, \infty) \to \mathbb{R}$ is an arbitrary function. In this work Gaussian RBFs will be used, defined as

$$\varphi_i(p) = \exp(-(\|p - p_i\|/\sigma_b)^2),$$

where σ_b stands for shape parameter. The Gaussian RBF are illustrated in Fig. 4. Many other types are known and used, with various recommendations [29].
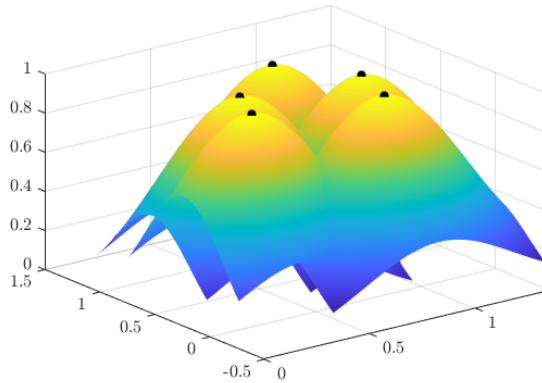

FIGURE 4 Gaussian radial basis functions with $\sigma_b = 0.5$ over a set of randomly generated nodes.

Imposing exactness of (6) for φ_k, we can write

$$(\mathcal{L}\varphi_k)(p_i) = \sum_{p_j \in \mathcal{N}(p_i)} w_j^i \varphi_k(p_j), \tag{8}$$

for all $p_k \in \mathcal{N}(p_i)$. Assembling all equations given by (8) in a matrix, the following system of equations is obtained:

$$\begin{bmatrix} \varphi(\|p_{j_1} - p_{j_1}\|) & \cdots & \varphi(\|p_{j_{n_i}} - p_{j_1}\|) \\ \vdots & \ddots & \vdots \\ \varphi(\|p_{j_1} - p_{j_{n_i}}\|) & \cdots & \varphi(\|p_{j_{n_i}} - p_{j_{n_i}}\|) \end{bmatrix} \begin{bmatrix} w_{j_1}^i \\ \vdots \\ w_{j_{n_i}}^i \end{bmatrix} = \begin{bmatrix} (\mathcal{L}\varphi_{j_1})(p_i) \\ \vdots \\ (\mathcal{L}\varphi_{j_{n_i}})(p_i) \end{bmatrix}, \tag{9}$$

where j_k are indices of nodes in $\mathcal{N}(p_i)$. Equation (9) is a system of n_i linear equations, compactly written as $A_i \boldsymbol{w}_i = b_i$, where matrix A_i is symmetric. Furthermore, the properties of such collocation matrices arising from radial basis functions have been

well studied[30,29]. If positive definite RBFs, such as Gaussian RBFs, are used, the matrices A_i are positive definite as soon as all nodes p_i are distinct[29]. Furthermore, to ensure consistency up to a certain order, RBF-FD approximation can be augmented with monomials. These consistency constraints are enforced using Lagrangian multipliers, resulting in a system similar to (9). For example, if a constant 1 is added to the basis set, the system for computing the weights reads

$$
\begin{bmatrix}
\varphi(\|p_{j_1} - p_{j_1}\|) & \cdots & \varphi(\|p_{j_{n_i}} - p_{j_1}\|) & 1 \\
\vdots & \ddots & \vdots & \vdots \\
\varphi(\|p_{j_1} - p_{j_{n_i}}\|) & \cdots & \varphi(\|p_{j_{n_i}} - p_{j_{n_i}}\|) & 1 \\
1 & \cdots & 1 & 0
\end{bmatrix}
\begin{bmatrix}
w^i_{j_1} \\
\vdots \\
w^i_{j_{n_i}} \\
\lambda^i_1
\end{bmatrix}
=
\begin{bmatrix}
(\mathcal{L}\varphi_{j_1})(p_i) \\
\vdots \\
(\mathcal{L}\varphi_{j_{n_i}})(p_i) \\
0
\end{bmatrix},
\tag{10}
$$

effectively adding an additional constraint $\sum_{i=1}^{n_i} w_{j_i} = 0$. The effects of adding polynomial constraints to RBF-FD approximations have been studied recently by Bayona et al.[7]. In cases discussed in this paper, additional consistency constraints were not needed to obtain satisfying results. Another possible modification to the RBF-FD above procedure is to include more stencil points then basis functions, putting basis functions only on the closest m_i nodes. This turns (9) into an underdetermined system, however, it can be solved uniquely by imposing additional condition of minimizing the norm $\|w_i\|$ of the weights. The benefit of this approach is that is less sensitive to perturbations of nodal positions[8]. This modification will be used in this paper.

After computing the coefficients w_i for all nodes, a sparse $N \times N$ matrix with $\sum_{i=0}^{N} n_i$ elements representing the governing problem can be assembled. The right hand side is computed from given f and u_0 and the sparse system is solved to obtain an approximation for u. Vector PDEs are treated as a coupled system of scalar PDEs, resulting in a proportionally larger system. Boundary conditions that involve differential operators, such as Neumann or traction boundary conditions, are discretised analogously to operator $\mathcal{L}$ above.

2.2.1 | Remarks on weight computation and shape parameter σ_b

It is worth noting that the selection of the shape parameter σ_b requires some attention. A known problem with computing the weights w_i is that as the shape parameter σ_b tends towards ∞, the accuracy increases, but the matrices A_i become more and more ill conditioned. A common solution is to scale the shape parameter σ_b proportionally to the internodal distance and thus keep condition numbers of A_i constant even as the node density increases. Another possible complication arises from the Runge Phenomenon, which comes into play with large σ_b and variable node densities. To avoid that, once again, a spatially variable shape parameter has been used as proposed by Fornberg and Zuev[19] and Flyer and Lehto[31].

A downside to using a spatially variable shape parameter, is that the matrices A_i (Eq. 9) lose their symmetry properties. To retain the symmetry, the shape parameter is kept constant for all entries in each A_i, but varies with i as $\sigma_{b,i} = \sigma_b \delta r_i$, where δr_i is the distance to the closest neighbouring node to p_i. Another downside is that scaled shape parameters may cause stagnation errors and failure of convergence[32], however no such problems were detected in cases discussed in this paper and scaling the shape parameter sufficed to suppress the Runge Phenomenon and mitigate ill-conditioning.

2.3 | Adaptive refinement

The refinement procedure presented in this paper is built on the following preliminaries.

(i) An a-posteriori error indicator $\hat{e}$ is known, where $\hat{e}(p)$ represents an indicator of error between an actual and computed value of some desired quantity at a point p. For convenience we define $\hat{e}(p_i) = \hat{e}_i$ for all $p_i \in \mathcal{P}$. In a more general setting $\hat{e}$ can also represent any kind of refinement indicator, with larger values indicating areas where refinement is needed and lower values indicating areas where it is unnecessary or even derefinement is possible.

(ii) Domain is initially filled with a known density $\delta r^{(0)}$.

(iii) Refinement is an iterative process that alters current radius function δr with respect to the error indicator.

(iv) The coarseness limit for δr is δr^u, i.e. the nodal radius during derefinement is bounded by δr^u_i from above.

(v) The nodal radius function δr is changed with respect to the density increase factor (f_i) that is evaluated based on the error indicator $\hat{e}_i$, the maximal (ε) and minimal (η) allowed error, and maximal (M) and minimal (m) value of the error indicator. The increase factor is limited to $f \in [1/\beta, \alpha]$, where $\alpha, \beta \geq 1$.

In each iteration the new nodal radii $\widetilde{\delta r}_i$ are computed as

$$\widetilde{\delta r}_i = \min(\delta r_i/f_i, \delta r_i^u), \tag{11}$$

where δr_i is the distance to from p_i to the closest neighbouring node. This imposes the upper bound on radii from point (iv) above. Similarly, a lower bound δr^ℓ limiting refinement could also be imposed, however in practice that bound was not needed. The density increase factor f_i is computed as

$$f_i = \begin{cases} 1 + \frac{\eta - \hat{e}_i}{\eta - m}\left(\frac{1}{\beta} - 1\right), & \hat{e}_i \leq \eta, \quad \text{i.e. decrease the density} \\ 1, & \eta < \hat{e}_i < \varepsilon, \quad \text{i.e. no change in density} \\ 1 + \frac{\hat{e}_i - \varepsilon}{M - \varepsilon}(\alpha - 1), & \hat{e}_i \geq \varepsilon, \quad \text{i.e. increase the density} \end{cases} \tag{12}$$

where $M = \max_{p_i \in \mathcal{P}} \hat{e}_i$ is the maximal and $m = \min_{p_i \in \mathcal{P}} \hat{e}_i$ the minimal value of the error indicator. The plot of factor f_i with respect to the error indicator $\hat{e}_i$ can be seen in Fig. 5 (left).
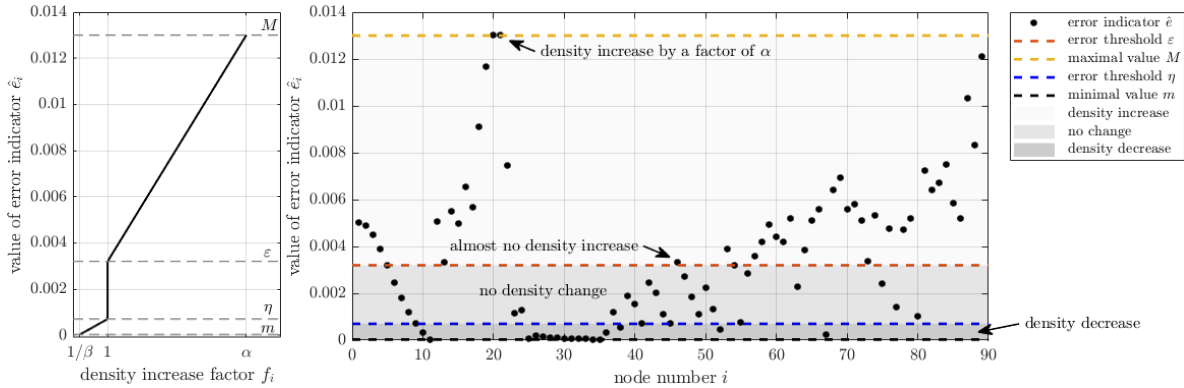

FIGURE 5 Construction of new density function $\widetilde{\delta r}$ from δr and $\hat{e}$.

Note that $\frac{1}{\beta} \leq f_i \leq \alpha$ always holds, as $\frac{\hat{e}_i - \varepsilon}{M - \varepsilon} \in [0, 1]$, and $\alpha \geq 1$. If the node is on the error threshold, i.e. $\hat{e}_i = \varepsilon$, the factor f_i equals 1 and the density will stay the same, ensuring compatibility with the case when $\hat{e}_i < \varepsilon$. Additionally, if the node has the highest error, i.e. $\hat{e}_i = M$, the increase factor will be maximal, i.e. α. Symmetric observations hold for the derefine case. Setting $\alpha = 1$ or $\beta = 1$ disables refinement or derefinement, respectively.

Once the desired nodal radii $\widetilde{\delta r}_i$ have been evaluated in all nodes, a new continuous function $\widetilde{\delta r}$ is reconstructed using Modified Sheppard's method as described in next Section 2.3.1. The overall density modification procedure is illustrated conceptually in Fig. 5.

2.3.1 | Computing the density function from given nodes

The positioning algorithm described in Section 2.1 requires continuous function δr as an input, while refinement algorithm described in Section 2.3 supplies discrete set of $\widetilde{\delta r}_i$ (11) known only in nodes. To construct a function $\delta r(p)$ from discrete values $\widetilde{\delta r}_i$, a Modified Sheppard's method is used. In a special case of $\alpha = \beta = 1$ this becomes an inverse problem of the node positioning problem described in Section 2.1. The problem is handled in a fairly straightforward manner, by defining local internodal distance δr_i for each node $p_i \in \mathcal{P}$ as

$$\delta r_i = \min_{\substack{p \in \mathcal{P} \\ p \neq p_i}} \|p_i - p\|. \tag{13}$$

The problem of computing the desired internodal distance at an arbitrary point $p \in \mathcal{P}$ translates to a problem of scattered data interpolation with known values δr_i at points p_i. Standard methods for this are well developed, described and compared by Franke[33]. Modified Shepard's method[33, p. 185] was used in this paper, where value of δr at a point p is computed as a weighted

sum of n closest neighbours of p

$$\delta r(p) = \begin{cases} \delta r_i, & \text{if } p = p_i \text{ for some } i \\ \frac{\sum_{i=1}^{n} w_i(p)\delta r_i}{\sum_{i=1}^{n} w_i(p)} & \text{else} \end{cases} \tag{14}$$

and the inverse distance weights $w_i(p)$ are defined by

$$w_i(p) = \left((1 - \frac{d_i}{d_n})\frac{1}{d_i} \right)^2, \tag{15}$$

where d_i represents the Euclidean distance from p to its i-th neighbour and the neighbours are sorted according to d_i, thus making d_n the largest.

There is however no need for interpolation of values δr_i, as they themselves are only an approximation, and techniques from scattered data approximation[34] might be more appropriate. We have tested different approximation and interpolation methods for values δr_i with no significant changes in characteristics of node distributions upon refilling the domain. Modified Sheppard's method was chosen based on computational efficiency and ease of implementation.

Every iteration of the adaptive procedure consists of filling the domain, solving the problem, and reconstructing and adapting the node density. Even without adaptation, these fill-reconstruction cycles do not guarantee the preservation of nodal density and it is therefore important to analyse their behaviour before implementing this approach into the refinement algorithm. To that end a continuation of the test case from Section 2.1 was performed to better asses the effects of the repeated application of fill-reconstruction cycles. The effects of 10 successive cycles on the initial nodal distribution are demonstrated in Fig. 6c.
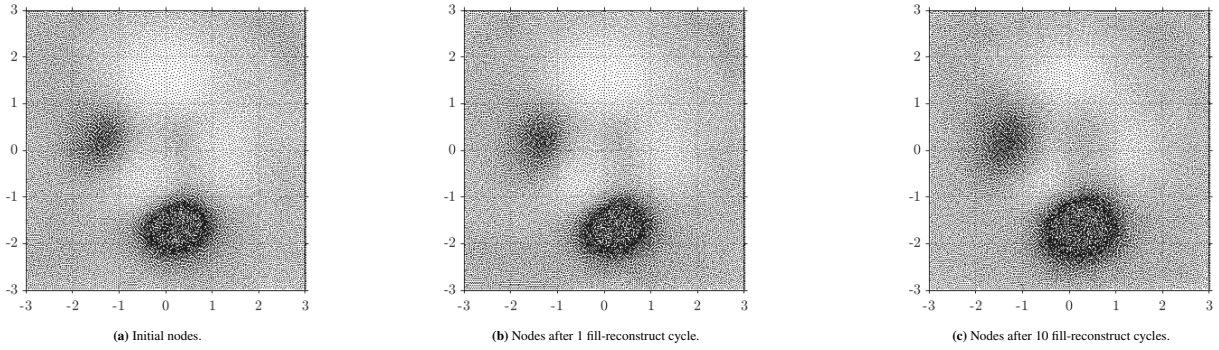

(a) Initial nodes.   (b) Nodes after 1 fill-reconstruct cycle.   (c) Nodes after 10 fill-reconstruct cycles.

FIGURE 6 Analysis of fill-reconstruct cycles.

Repeated application of fill-reconstruction cycles tends to slightly increase the nodal density, due to the proximity factor that is set to $\zeta = 0.99$. After 1 iteration, the minimal internodal distance is reduced from 0.00699727 to 0.00697768 and after 10 iterations to 0.00688613, i.e. a reduction of 1.5% over the course of 10 iterations, which is well within the allowed limit of 1% per iteration, as imposed by the fill tolerance factor ζ. The most visible effect of successive application is the gradual spread and smear of high density areas, which expand with every successive iteration. This feature would be undesirable in certain situations and can be dealt with, however in numerical examples presented in this paper the phenomenon did not have considerable impact and is therefore not discussed further.

3 | NUMERICAL RESULTS

3.1 | Governing problem

The solution procedure presented in previous section is applied to linear elasticity contact problems, more precisely to problems of deformation of elastic homogeneous isotropic materials under load. The problem is governed by Cauchy-Navier equations

$$(\lambda + \mu)\nabla(\nabla \cdot \vec{u}) + \mu\nabla^2\vec{u} = \vec{f}, \tag{16}$$

where $\vec{u}$ are unknown displacements, $\vec{f}$ is the loading body force, and λ and μ are Lamé parameters, often expressed in terms of Young's modulus E and Poisson's ratio ν. Another important quantity is the stress tensor σ, related to strain via Hooke's law

$$\sigma = \lambda \operatorname{tr}(\varepsilon)I + 2\mu\varepsilon, \quad \varepsilon = \frac{\nabla\vec{u} + (\nabla\vec{u})^{\mathsf{T}}}{2}, \tag{17}$$

where λ and μ are Lamé parameters from above and I is the identity tensor.

Two types of boundary conditions are considered: essential boundary conditions which specify displacements on some portion of the boundary of the domain, i.e. $\vec{u} = \vec{u}_0$, and traction boundary conditions, which prescribe surface traction $\sigma\vec{n} = \vec{t}_0$, with $\vec{n}$ being an outside unit normal to the boundary of the domain.

In two dimensions, we will use the following componentwise notation for $\vec{u}$ and σ, for sake of simplicity:

$$\vec{u} = (u, v) \quad \text{and} \quad \sigma = \begin{bmatrix} \sigma_{xx} & \sigma_{xy} \\ \sigma_{xy} & \sigma_{yy} \end{bmatrix}. \tag{18}$$

3.2 | Disk under pressure

To demonstrate the adaptive strategy from Section 2.3, a 2D example from linear elasticity, inspired by [35], is chosen. A disk of radius R is subjected to diametrical compression with a point force of magnitude P, as illustrated in Fig. 7.
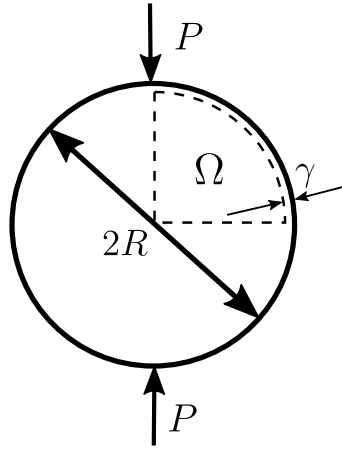

FIGURE 7 Disk under diametrical compression.

Exact closed form solution for stresses, assuming plane stress condition, is known, given by e.g. Sadd [36, p. 197] as:

$$\sigma_{xx} = -\frac{2P}{\pi}\left(\frac{x^2(R-y)}{r_1^4} + \frac{x^2(R+y)}{r_2^4} - \frac{1}{2R} \right) \tag{19}$$

$$\sigma_{yy} = -\frac{2P}{\pi}\left(\frac{(R-y)^3}{r_1^4} + \frac{(R+y)^3}{r_2^4} - \frac{1}{2R} \right) \tag{20}$$

$$\sigma_{xy} = \frac{2P}{\pi}\left(\frac{x(R-y)^2}{r_1^4} - \frac{x(R+y)^2}{r_2^4} \right) \tag{21}$$

where $r_{1,2} = \sqrt{x^2 + (R \mp y)^2}$ are the distances to the poles. The stress distribution is singular at the poles.

Numerically, only a quarter of the disk is considered due to symmetry. Additionally, a small boundary layer of width γ is subtracted from the curved edge of the domain, to avoid the singularity at the poles. Therefore, the computational domain Ω, shown in Fig. 7, is a quarter of a circle with radius $R - \gamma$. The parameter γ determines the peak stress magnitudes of order $\frac{P}{2\pi\gamma}$ concentrated around the point $x = 0$, $y = R - \gamma$, allowing fine control over case difficulty. Thus the following problem is solved:

$$(\lambda + \mu)\nabla(\nabla \cdot \vec{u}) + \mu\nabla^2\vec{u} = 0 \quad \text{in} \quad \Omega = \{(x, y) \in \mathbb{R}^2; \ x \geq 0, y \geq 0, x^2 + y^2 \leq (R - \gamma)^2\}. \tag{22}$$

Traction boundary conditions are imposed on the curved boundary, given by equations (19–21). Symmetry boundary conditions $v = 0, \frac{\partial u}{\partial y} = 0$ and $u = 0, \frac{\partial v}{\partial x} = 0$ are imposed on the bottom and left boundary, respectively.

Three possible values for γ will be considered, $\gamma_1 = 0.2$, $\gamma_2 = 0.02$ and $\gamma_3 = 0.002$. The values of the stresses along the antidiagonal $x = R - \gamma - y$ of Ω are shown in Fig. 8.
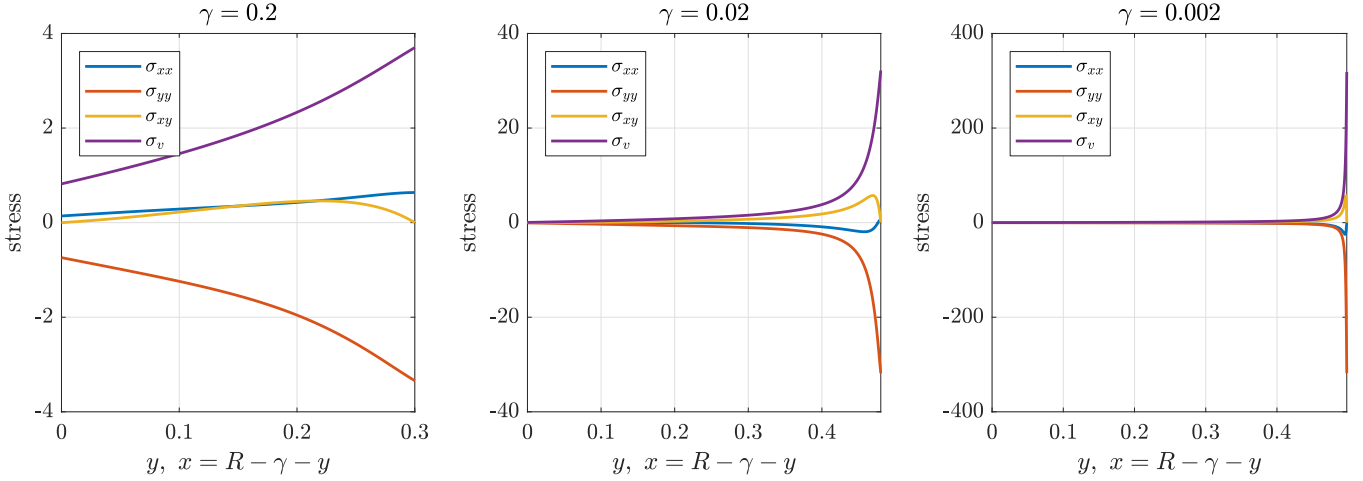

FIGURE 8 Stress values along the antidiagonal $x = R - \gamma - y$ for three different cases.

The error between analytical stresses σ and computed stresses $\hat{\sigma}$ is measured in three different ways:

- Relative approximate L^∞ norm:

$$e_\infty = \frac{\|\hat{\sigma} - \sigma\|_\infty}{\|\sigma\|_\infty}, \quad \|\sigma\|_\infty = \max_{p \in \Omega_h} \max\{\sigma_{xx}(p), \sigma_{yy}(p), \sigma_{xy}(p)\} \tag{23}$$

- Relative approximate L^1 norm:

$$e_1 = \frac{\|\hat{\sigma} - \sigma\|_1}{\|\sigma\|_1}, \quad \|\sigma\|_1 = \frac{1}{3|\Omega_h|} \sum_{p \in \Omega_h} (|\sigma_{xx}(p)| + |\sigma_{yy}(p)| + |\sigma_{xy}(p)|) \tag{24}$$

- Relative energy norm:

$$e_E = \frac{\|\hat{\sigma} - \sigma\|_E}{\|\sigma\|_E}, \quad \|\sigma\|_E^2 = \int_\Omega \tilde{e}_E(p)\,d\Omega, \quad \tilde{e}_E(p) = \sigma(p) : S : \sigma(p), \tag{25}$$

where S is the fourth-order compliance tensor computed from E and v.

The norms are evaluated by discretising Ω with a dense uniform grid Ω_h with grid spacing $h = 5 \cdot 10^{-4}$, resulting in around 800 000 grid points. For e_∞ and e_1 the maximum and the sum are taken over these grid points. The intermediate values of $\sigma(p)$ for $p \notin \mathcal{P}$ were evaluated using linear interpolation over the Delaunay triangulation induced by the points in $\mathcal{P}$. The integral in e_E was approximated using trapezoidal rule over Ω_h.

Adaptive approach, described in Section 2.3 is now employed to solve problem (22). The error indicator is constructed from the known analytical solution (19–21), using the kernel of the integral for energy norm (25) multiplied by the approximation of the volume element

$$\hat{e}(p) = (\sigma(p) : S : \sigma(p))\delta r(p)^d, \tag{26}$$

where $d = 2$ is the dimension of the problem.

To discretise the domain, fill algorithm from Section 2.1 with $\zeta = 0.9$ was used and the distribution was regularised using repel algorithm with $N_r = 10$ iterations, $Q_i = 0.8$, $Q_j = 0$, $\kappa = 2$ and 3 neighbours. The domain was initially filled with constant density of $\delta r^{(0)} = 0.02$, amounting to approximately $N = 600$ nodes in the domain. For the given discretisation, RBF-FD with 25 neighbouring nodes and 15 Gaussian RBFs was used. The shape parameter σ_b was varied proportionally to the

internodal distance with base value $\sigma_b = 100$. For adaptive iteration, $\varepsilon = 10^{-7}$, $\eta = 10^{-9}$, $\alpha = 5$ and $\beta = 1.5$ were chosen. The reconstruction and evaluation of the new density function $\widetilde{\delta r}$ was done using 7 closest neighbours. Values of $R = 0.5$, $P = 1$, $E = 1$ and $\nu = 0.33$ were taken for physical parameters of the problem.

The overall procedure seems to depend on a lot of free parameters, however most are either well studied, such as the RBF shape parameters (see Section 2.2.1) or their value is not very important to the overall procedure, such as the fill, repel and reconstruct parameters, described in more detail in Sections 2.1 and 2.3.1. Standard values, as described above and as used by Slak and Kosec [8], were taken for these parameters and they were kept the same for all runs, to avoid hyper-tuning the results. The parameters related to adaptivity are further analysed in Section 3.3 and justify the choices above.

The stress profiles computed with the presented adaptive procedure for all three cases are shown in Fig. 9. To avoid cluttering, only σ_{xy} stress component is shown, but all behave similarly. In the first case, the initial distribution is almost sufficiently dense and thus adaptive procedure finishes after 2 iterations. The lower panel still reveals gradual improvement in both iterations. In the second case, the initial solution underestimates the peak stress value, the next iteration overestimates it, but then the profiles start to match with the analytic profile, as seen in the lower panel. This behaviour is even more prominent in the final case, where the initial distribution covers high stress area very coarsely and the first few iterations are only beginning to accurately cover the narrow stress peak. The lower panel once again shows that in the later iterations, when the solution behaviour has been well captured, the procedure behaves similarly to the other cases.
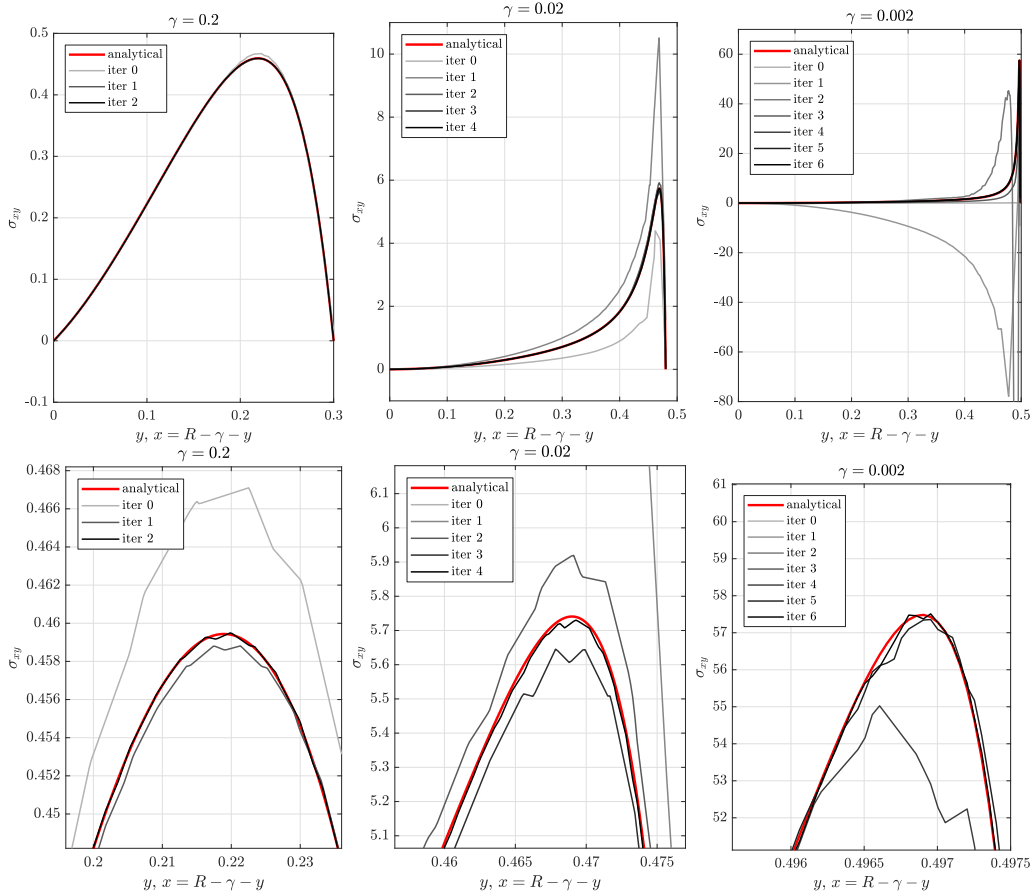

FIGURE 9 Computed σ_{xy} stress profiles for three considered cases. The lower three images show close-ups of the computed peaks.

The errors over the course of the adaptive iteration are shown in Fig. 10 and confirm the behaviour observed in Fig. 9. All three error norms decrease as the algorithm proceeds, however no guarantee of monotonicity is given and sudden jumps in error can happen. In the second and more prominently in the third case, an initial rise in error can be observed, caused by low initial

nodal densities. However in few iterations, the algorithm increases the density enough to accurately detect the error regions. Note that the error threshold ε has no direct connection to the final errors observed, only a general rule that lowering ε will also decrease the measured errors holds. The number of nodes is also shown and behaves as expected: mode difficult cases require more iterations to obtain the final solution, which also uses more nodes for harder cases.
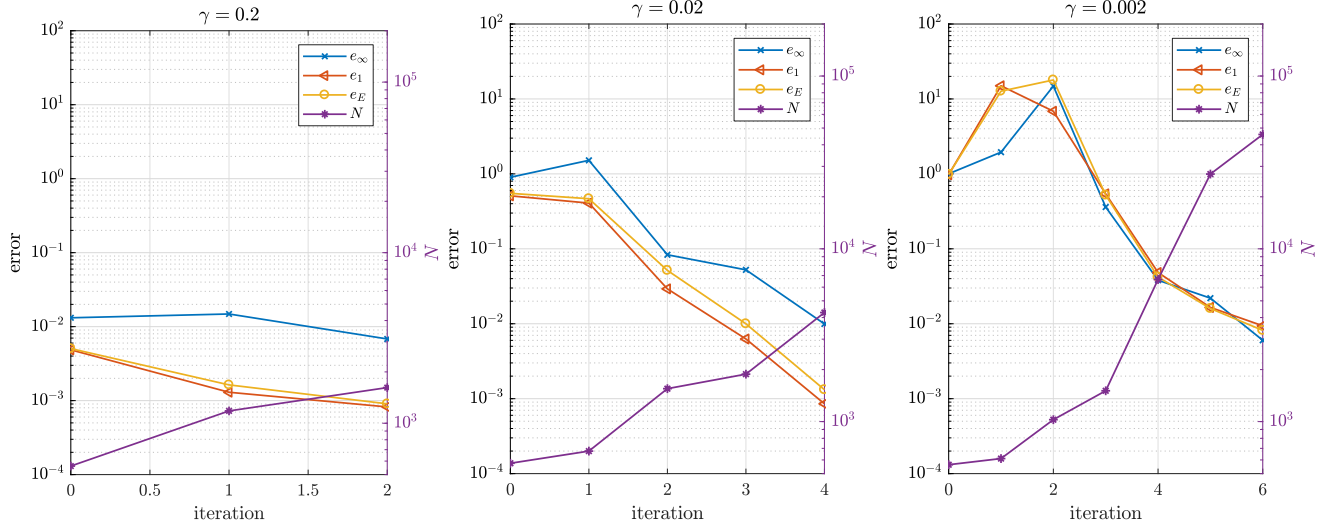

FIGURE 10 Error of the numerical solution with respect to adaptive iteration.

To better visualise the adaptive results, a comparison between initial and final values of errors, error indicator and nodal densities are shown in Fig. 11.
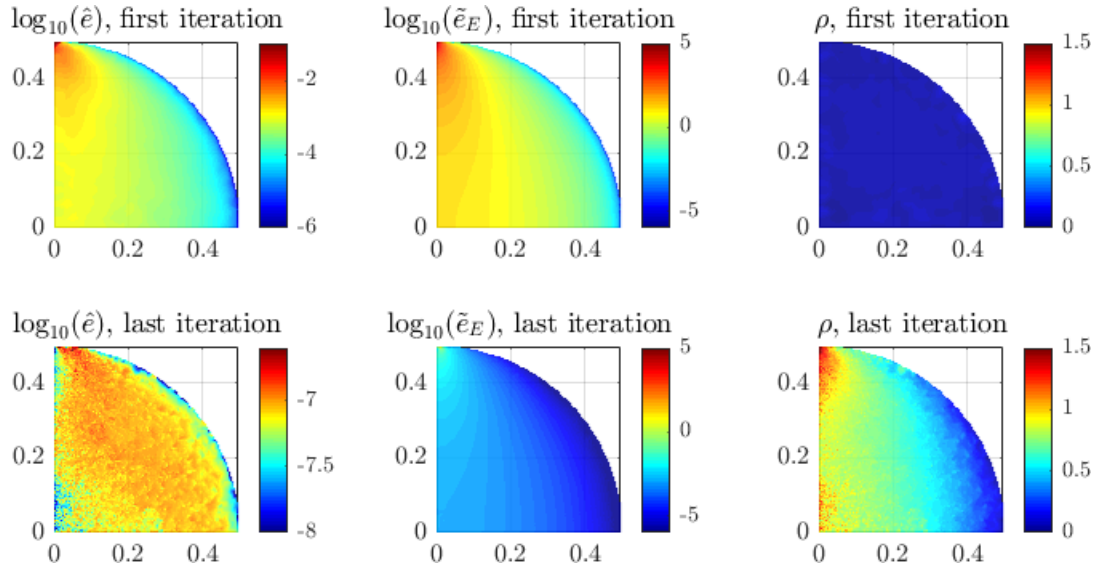

FIGURE 11 Error indicator value in the last iteration.

The measure of relative nodal density ρ at p_i is defined as

$$\rho_i = -\log_{10}(\delta r_i / \max_i(\delta r_i)), \tag{27}$$

where δr_i is the distance to the closest neighbouring node. A value of e.g. $\rho_i = 2$ means that nodal density around node p_i is 10^2 times greater than the lowest density in the domain. For the measure of error at node p_i the kernel of the energy error $\tilde{e}_E$ (25) was taken. Initially the nodal density is constant (i.e. $\rho \approx 0$) and the error and error indicator approximately match (up to a factor). In the last iteration, the error indicator is more uniformly distributed over the whole domain and its value is lower in general, as expected. When comparing the error and nodal densities the same colour axis limits were used for the first and the last iteration to get a correct global impression. Over the course of the adaptive iteration the high error areas were repeatedly refined, gradually lowering the error to a much more uniform distribution. The final density distribution however transformed opposite to the error, from a uniform distribution to the final distribution that resembles the initial error distribution. This mutually reverse transition to and from uniformity between error and node density was observed in all three considered cases.

Finally, to justify testing the adaptivity on these cases at all, the problem (22) is solved with uniform node density, i.e. the density function δr is constant. Error of the numerical solution was analysed for δr ranging from 0.05 to 0.0033. The results for all three cases are shown in Fig. 12.
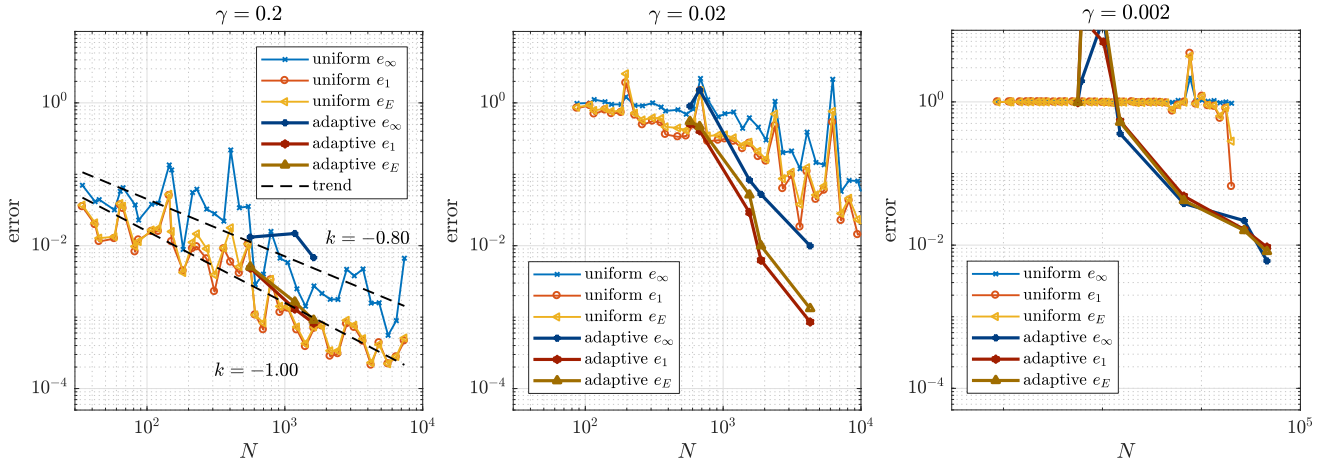

FIGURE 12 Error of the numerical solution with respect to number of nodes.

The value of parameter γ clearly influences the case difficulty and the need for adaptivity. In the easiest case uniformly distributed nodes perform well, and the observed order of convergence in e_∞ matches expectations provided by the theory for standard finite difference approximations. The middle case however exhibits worse convergence properties, and the method completely fails to even compute the most difficult case with satisfiable accuracy. Adaptivity is clearly needed in the last two cases and the tested procedure displays satisfactory error behaviour in all three cases.

3.3 | Analysis of adaptivity parameters

The two important parameters of the refine procedure are the error threshold ε and refine aggressiveness α. The error threshold parameter ε is straightforward, and it generally holds that the lower the ε, the lower the final error will be. Note that if $\hat{e}$ is merely an error indicator and not an error estimator (i.e. it only gives an indication of areas with high errors and not upper bounds on errors), then the final error may be larger than ε.

The parameter α controls the aggressiveness of the refine procedure, as it bounds the density increase from above by a factor of at most α. Setting e.g. $\alpha = 2$ allows the internodal distance to at most halve and the number of nodes in a region to increase at most 4 times (in 2D). Intuitively, lower values of α should result in slower and more controlled error decreases, while higher values lower the number of needed iterations but the error behaviour is more volatile.

To analyse the behaviour with respect to α the case $\gamma = \gamma_2$ was solved using the same parameters as in Section 3.2, while α ranged from 1.1 to 100. Fig. 13a shows the number of adaptive iterations until convergence, i.e. the number of while loop iterations on line 5 in algorithm 1. The missing data points indicate failure of convergence.

As predicted, the number of iterations reduces steadily with larger α up to around $\alpha = 10$ when the behaviour becomes too unstable and failures of convergence occur often. In the stable region with $\alpha \lesssim 10$ both the number of nodes in the final iteration
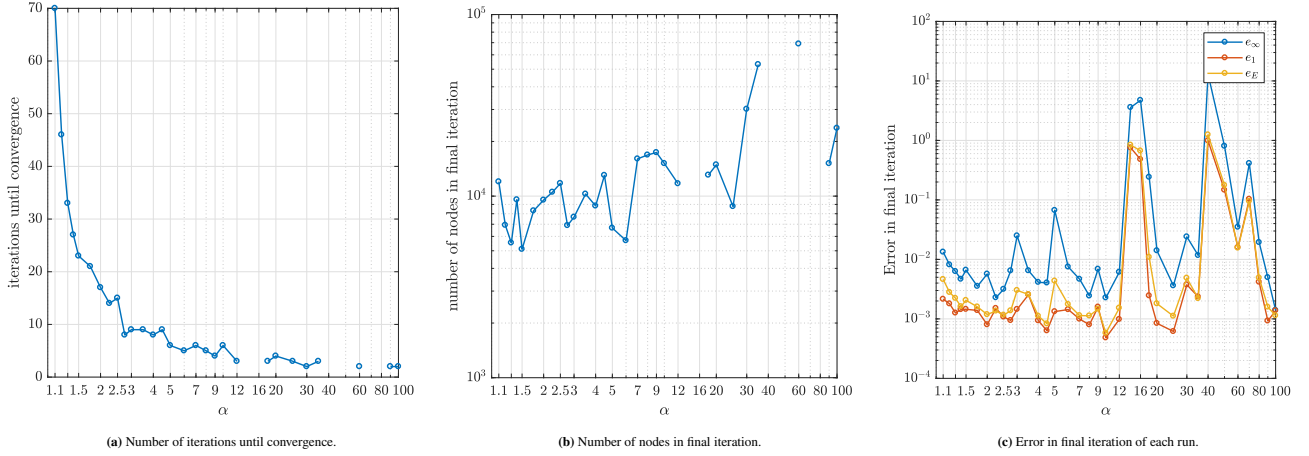
(a) Number of iterations until convergence.

(b) Number of nodes in final iteration.

(c) Error in final iteration of each run.

FIGURE 13 Analyses of effect of aggressiveness parameter α. Missing data points indicate a divergent solution.

(Fig. 13b) and the error in the final iteration (Fig. 13c) are mostly independent of α, meaning that irrespective of how many iterations it took to get to a satisfiable solution, the solution has approximately the same error and uses approximately the same number of nodes. Therefore, to reduce the number of iterations necessary while being safely on the stable side, $\alpha = 5$ was chosen.

The corresponding derefine parameters β and η behave similarly to α and ε. Too large values of β cause volatile behaviour, while too low values simply mean that some areas may be covered with too many nodes, which has little effect on convergence but unnecessarily increases computational costs. Usually the value of $\beta = 1.5$ was chosen to derefine more conservatively. The initial distribution $\delta r^{(0)}$ was usually chosen for the coarseness bound δr^u. This means that derefine cannot reduce the density in the first few iterations, but can still correct possible increases in wrong areas later on.

The remaining free parameters are related to the density reconstruction (see sec. 2.3.1) using modified Sheppard's method. Varying the number of neighbours n from 3 to 15 had no significant effect on the solution procedure. Weighting over $n = 7$ nodes was used in most runs.

3.4 | Hertzian contact

The next case considers Hertzian contact between an elastic cylinder and a half plane, as recently used by Slak and Kosec[8]. The analytical boundary condition on the top boundary is given by the known pressure distribution

$$p(x) = \begin{cases} p_0 \sqrt{1 - \frac{x^2}{a^2}}, & |x| \leq a \\ 0, & \text{otherwise} \end{cases}, \qquad p_0 = \sqrt{\frac{P E^*}{\pi R}}, \quad a = 2\sqrt{\frac{P R}{\pi E^*}}, \tag{28}$$

where P is the pressure force, R is the radius of the cylinder and the combined Young's modulus E^* is given by $\frac{1}{E^*} = \frac{1-v_1^2}{E_1} + \frac{1-v_2^2}{E_2}$, where E_1, v_1 and E_2, v_2 are the material properties of the cylinder and the half plane, respectively. The remaining boundary conditions are no-displacement conditions at infinity.

The problem is solved numerically by truncating the half plane to a rectangle $[-H, 0] \times [-H, H]$ and applying the no displacement boundary conditions at all boundaries but the top, as illustrated in Fig. 14. For the choice $R = 1$ m, $P = 543 \, \text{N/m}$, $E = 72.1$ GPa, $v = 0.33$, the contact width a is approximately 0.13 mm. A choice of $H = 0.1$ m, which is approximately 770 times larger than the phenomenon of interest, is sufficiently large that the truncation error does not present a significant contribution[8].

The large ratio between domain size and contact width presents a challenging case for adaptive refinement algorithms. The domain was initially filled with a constant discretisation step h, using the filling algorithm described in section 2.1. The initial step h needs to be small enough to capture the contact itself, while this same h might be unnecessarily small for the rest of the domain. This offers a chance to demonstrate adaptive derefinement as well.

Additionally, instead of an analytical indicator given by (26), a simple ad-hoc error indicator was tested, to develop a functional indicator for cases where no analytical solution is available.
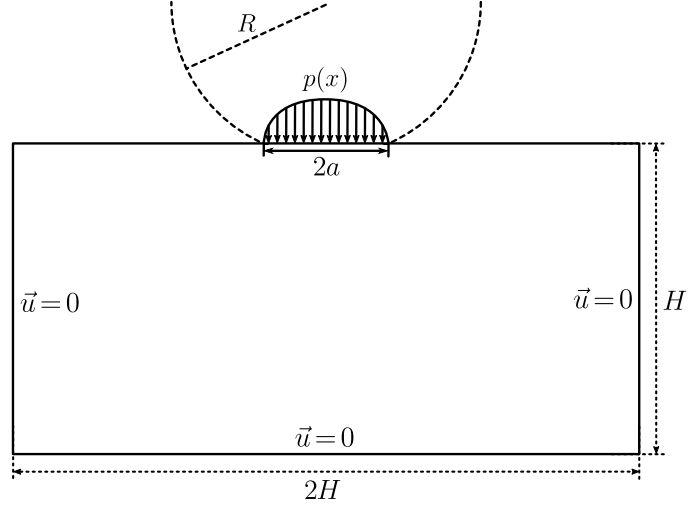
FIGURE 14 Numerical domain and boundary conditions for the solution of Hertzian contact problem.

The construction of the indicator starts on the premise that the discretisation needs to be refined in areas with high gradients, i.e. the areas where the variability of the numerical solution is locally large. Therefore a simple indicator such as standard deviation of the solution over local support domain

$$\hat{e}_i = \operatorname*{std}_{p_j \in N_i} \sigma_{xx}(p_j) + \operatorname*{std}_{p_j \in N_i} \sigma_{yy}(p_j) + \operatorname*{std}_{p_j \in N_i} \sigma_{xy}(p_j), \tag{29}$$

was tested.

The adaptive procedure was run with $\alpha = 5$, $\varepsilon = 10^5$, $\beta = 1.5$, $\eta = 10^4$ and left to run for 6 iterations. The errors measured against a closed form solution[8, eq. (54–56)] and the number of nodes over the course of the iterative procedure are shown in Fig. 15. Additionally, data about node refinement for each iteration is shown in Table 1.
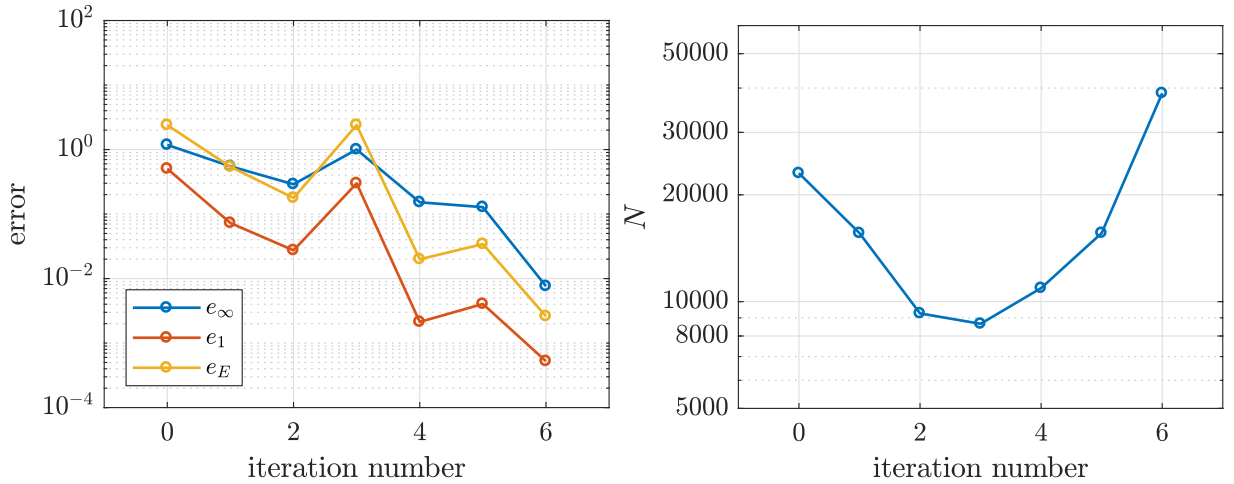

FIGURE 15 Errors and node counts during iteration.

In the beginning, the derefinement is substantial and the node count decreases, however, refinement is already present for nodes under contact. Later in the procedure, refinement becomes more pronounced and the total number of nodes increases. The computed top surface tractions over the course of the adaptive iteration are shown in Fig. 16.

It is interesting to compare these results to the manually refined solution obtained by Slak and Kosec[8]. The error in the final iteration of the adaptive procedure is in the same range as the errors obtained by manual refinement. Additionally, an interesting

iteration	total nodes	refined	no change	derefined	derefined, but hit bound δr^u
0	23 012	384	3 427	19 201	0
1	15 596	483	777	14 336	0
2	9 264	1 127	1 469	6 668	0
3	8 658	5 198	3 460	0	0
4	10 918	3 097	2 017	5 804	0
5	15 605	9 494	2 189	3 753	169
6	38 674	/	/	/	/

TABLE 1 Number of refined and derefined nodes for each iteration.
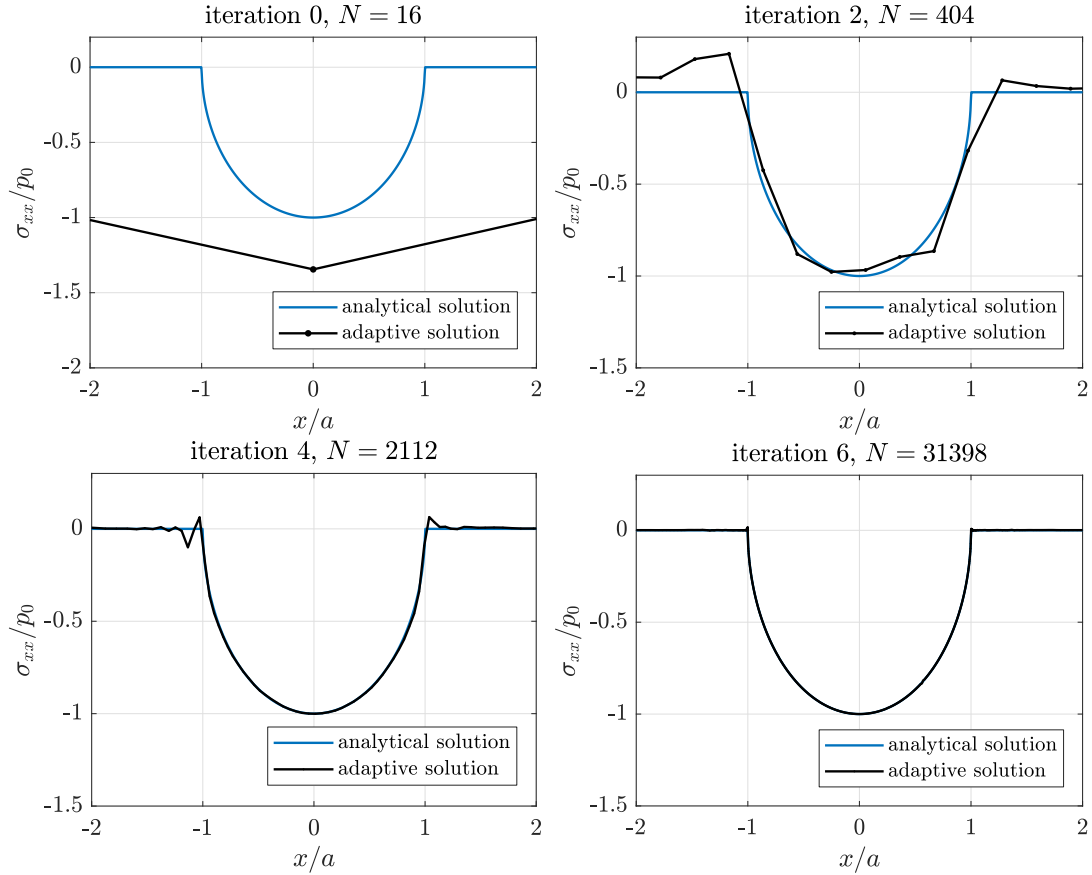
FIGURE 16 Top surface stress profiles during the iteration. Only even iterations are shown for brevity.

comparison of node densities under contact can be made and is shown in Fig. 17. The manual and adaptively obtained densities generally refine the same areas, however the adaptively obtained density is much smoother.

From the error plot in Fig. 15 and the density plot in Fig. 17 it can be concluded that the error indicator $\hat{e}$, given by (29), works adequately in practice.
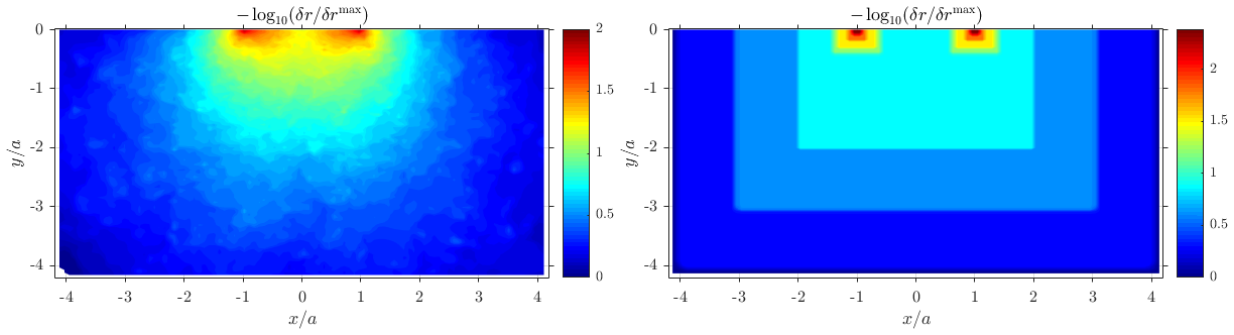
FIGURE 17 Comparing adaptive (left) and manual (right) nodal distributions densities.

3.5 | Fretting fatigue contact

The usability of the described adaptive technique is further demonstrated on a case, originating from the study of fretting fatigue, described by Pereira et al. [27], for which the authors believe no closed form solution is known. A small thin rectangular specimen of width W, length L and thickness t is stretched in one axis with axial traction σ_{ax} and compressed in another with force F by two oscillating cylindrical pads of radius R, inducing tangential force Q, as shown in Fig. 18a. The tractions induced by the pads are predicted using an extension of Hertzian contact theory, which splits the contact area into the stick and slip zones, depending on the coefficient of friction μ and combined Young's modulus E^*, given by $\frac{1}{E^*} = \frac{1-\nu_1^2}{E_1} + \frac{1-\nu_2^2}{E_2}$, where E_i and ν_i represent the Young's moduli and Poisson's ratios of the specimen and the pad, respectively. The theory predicts the contact half-width

$$a = 2\sqrt{\frac{FR}{t\pi E^*}}, \tag{30}$$

normal traction

$$p(x) = \begin{cases} p_0\sqrt{1 - \frac{x^2}{a^2}}, & |x| < a \\ 0, & \text{else} \end{cases}, \qquad p_0 = \sqrt{\frac{FE^*}{t\pi R}}, \tag{31}$$

and tangential traction

$$q(x) = \begin{cases} -\mu p_0 \left(\sqrt{1 - \frac{x^2}{a^2}} - \frac{c}{a}\sqrt{1 - \frac{(x-e)^2}{c^2}} \right), & |x - e| < c \\ -\mu p_0 \sqrt{1 - \frac{x^2}{a^2}}, & c \le |x - e| \text{ and } |x| \le a \\ 0, & \text{else} \end{cases} \tag{32}$$

where $c = a\sqrt{1 - \frac{Q}{\mu f}}$ is the half-width of the slip zone, and $e = \text{sgn}(Q)\frac{a\sigma_{ax}}{4\mu p_0}$ is the eccentricity due to axial loading. Note that the inequalities $Q \le \mu F$ and $\sigma_{ax} \le 4\left(1 - \sqrt{1 - \frac{Q}{\mu F}}\right)$ must hold for these expressions to be valid, both of which will be satisfied in our case.

Plane strain is used to reduce the problem to two dimensions and symmetry along the horizontal axis is used to reduce the problem size. The region $\Omega = [-L/2, L/2] \times [-W/2, 0]$ is taken as the problem domain and the boundary conditions are illustrated in Fig. 18b.

Values of $E_1 = E_2 = 72.1$ GPa, $\nu_1 = \nu_2 = 0.33$ were taken for the material parameters, coinciding with aluminium 2420-T3. Dimensions of the specimen were $L = 40$ mm, $W = 10$ mm and $t = 4$ mm. Values $F = 543$ N, $Q = 155$ N, $\sigma_{ax} = 100$ MPa, $R = 10$ mm and $\mu = 0.3$ were chosen for the model parameters. This means that the half-contact width a equals 0.2067 mm, which is approximately 200 times smaller than the domain width W, once again making it difficult to solve without adaptivity. The same ad-hoc error indicator as in Section 3.4 was used to adaptively refine the solution. The initial distribution was generated using constant spacing $\delta r^{(0)} = 0.5$ mm, putting exactly one node on the whole contact surface. 4 iterations of the adaptive solution procedure were run using $\varepsilon = 0.1$ MPa as the error threshold and $\alpha = 10$, resulting in a domain populated with 49 993 nodes. The sets of nodes $\mathcal{P}$ and the corresponding numerical solutions obtained during the adaptive iteration are shown in Fig. 19. The results are compared to a solution obtained with the Finite Element Method (FEM) on a much denser mesh with more than 100 000 DOFs, using commercial ABAQUS® software for finite element analysis, where manual refinement has been
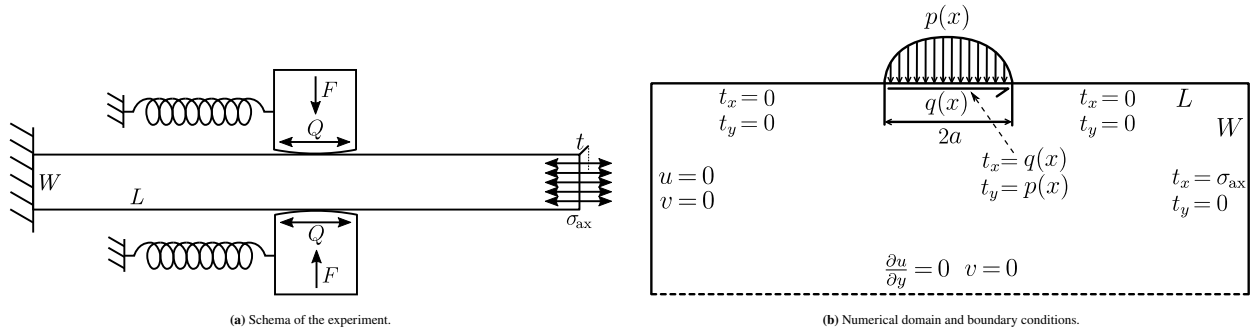
FIGURE 18 Description of the considered case. Ratios in the drawings are not to scale.

used [27], as well as to another FEM solution, obtained using the freely available FreeFem++ [37] and its built-in adaptive refinement techniques.
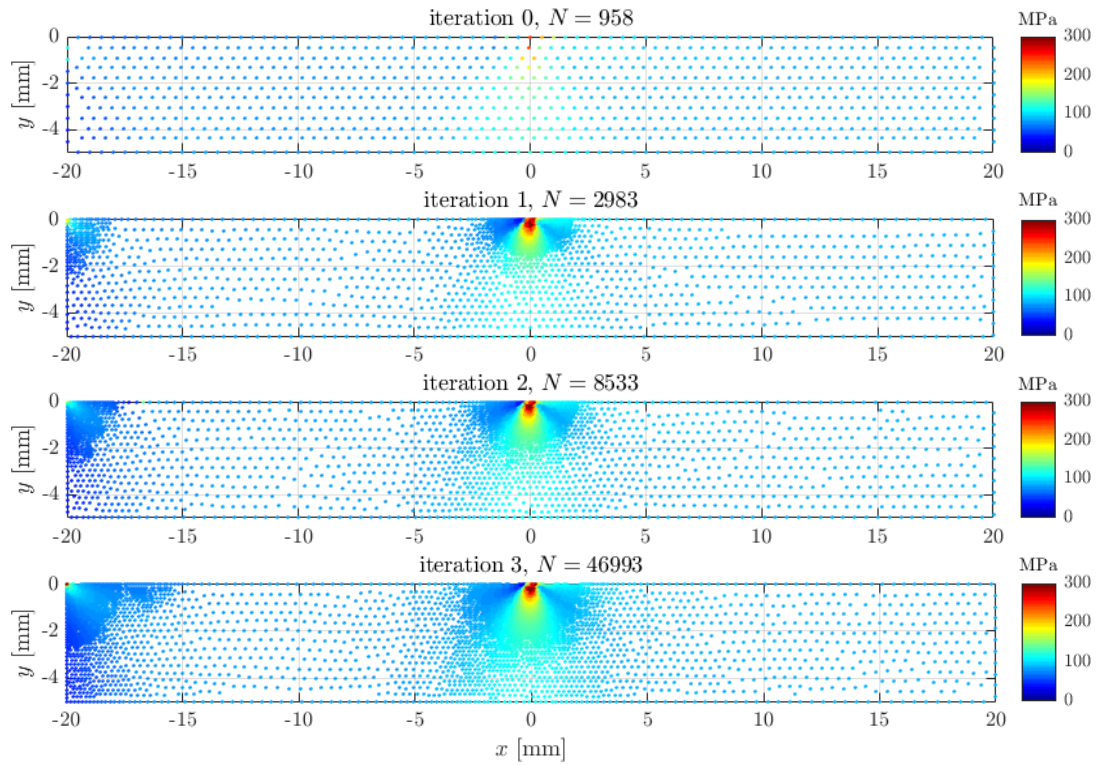

FIGURE 19 Nodes of four subsequent adaptive iterations, coloured by von Mises stress.

The surface traction σ_{xx} is of particular interest, as it is often used to determine the location of crack initiation [27]. Its graph over the course of the adaptive iteration is shown in Fig. 20. In the initial solution, only one node is placed under the contact surface; however, after the final iteration, there are approximately 700 nodes under the contact surface and the results agree well with FEM solutions.

Additionally, error of the adaptive solution is shown in Fig. 21. The error was measured using e_1 (see Eq. 24) on the contact surface, specifically on the interval $[-2a, 2a]$, where a is the contact half width. As no analytical solution is known, the error was measured using reference FEM solutions.
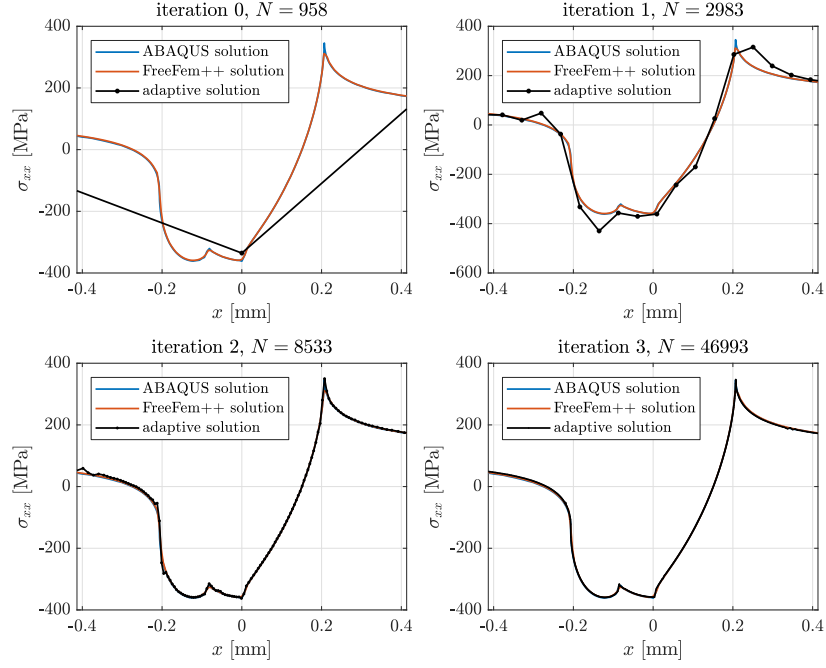
FIGURE 20 Surface traction σ_{xx} under contact in four subsequent adaptive iterations.
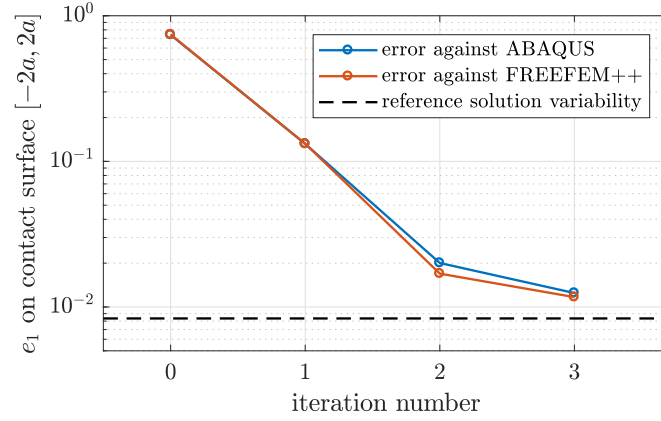
.

FIGURE 21 Error of surface traction using two reference solutions.

.

The two reference solutions were computed to also asses the variability between solutions obtained with established methods and implementations, and our adaptive implementation. The error shown in Fig. 21 decreases with each iteration, similarly to other already presented cases, and achieves satisfactory accuracy, nearing the reference solution variability.

4 | CONCLUSIONS

Adaptive refinement is a crucial part of a numerical solution procedure for any problem that exhibits extensive differences in intensity within the problem domain. In this paper, a modular adaptive refinement algorithm for solving elliptic boundary value problems was proposed. The refinement procedure consists of Poisson Disc Sampling based nodal positioning algorithm, a meshless solution using RBF-FD of the governing problem, the refinement strategy, and the reconstruction of the density function needed to redistribute the points. The free parameters of the algorithm were determined by means of numerical experiments,

and reasonable defaults along with acceptable intervals were proposed. Finally, it was clearly demonstrated that the proposed algorithm provides a stable solution for all considered cases without any hyper-tuning. The most convincing was the solution of the fretting fatigue case, where complications arise due to the presence of the stick-slip zone at the contact interface, which causes extreme peaks in surface stress making it very difficult to solve numerically in reasonable time without refinement. The proposed approach successfully adaptively refined initially uniform discretisation, captured both peaks, and numerically solved the problem in only four iterations, with excellent agreement towards the reference solution provided by commercial software using manual refinement.

Although all discussions in this paper were limited to the consideration of the Navier-Cauchy partial differential equation and contact problems, the presented methodology can also be applied in other areas where numerical discretisation is required to solve the governing problem. The only notable required change would be in the second step, i.e. the solution of the problem, while the other steps would remain the same. Furthermore, all elements of the algorithm have no intrinsic dependency on the dimensionality of the space, therefore the generalisation to 3D can be done in a straightforward manner, which is a goal for future research.

5 | ACKNOWLEDGEMENTS

References

1. Kansa EJ. Multiquadrics – A scattered data approximation scheme with applications to computational fluid-dynamics – I surface approximations and partial derivative estimates. *Computers & Mathematics with applications* 1990; 19(8-9): 127–145. doi: 10.1016/0898-1221(90)90270-T

2. Franke C, Schaback R. Solving partial differential equations by collocation using radial basis functions. *Applied Mathematics and Computation* 1998; 93(1): 73–82. doi: 10.1016/s0096-3003(97)10104-7

3. Šarler B. *From global to local radial basis function collocation method for transport phenomena*: 257-282; Berlin: Springer . 2007.

4. Prax C, Sadat H, Salagnac P. Diffuse approximation method for solving natural convection in porous media. *Transport in Porous Media* 1996; 22: 215-223. doi: 10.1007/bf01143516

5. Tolstykh A, Shirobokov D. On using radial basis functions in a "finite difference mode" with applications to elasticity problems. *Computational Mechanics* 2003; 33(1): 68–79. doi: 10.1007/s00466-003-0501-9

6. Fornberg B, Flyer N. Solving PDEs with radial basis functions. *Acta Numerica* 2015; 24: 215–258. doi: 10.1017/S0962492914000130

7. Bayona V, Flyer N, Fornberg B, Barnett GA. On the role of polynomials in RBF-FD approximations: II. Numerical solution of elliptic PDEs. *Journal of Computational Physics* 2017; 332: 257–273. doi: 10.1016/j.jcp.2016.12.008

8. Slak J, Kosec G. Refined Meshless Local Strong Form solution of Cauchy–Navier equation on an irregular domain. *Engineering Analysis with Boundary Elements* 2018. doi: 10.1016/j.enganabound.2018.01.001

9. Kosec G. A local numerical solution of a fluid-flow problem on an irregular domain. *Adv. Eng. Software* 2018; 120: 36-44. doi: 10.1016/j.advengsoft.2016.05.010

10. Fornberg B, Flyer N. Fast generation of 2-D node distributions for mesh-free PDE discretizations. *Computers & Mathematics with Applications* 2015; 69(7): 531–544. doi: 10.1016/j.camwa.2015.01.009

11. Belytschko T, Liu WK, Singer M. *On adaptivity and error criteria for meshfree methods*. 47. : 217-228; Elsevier . 1998.

12. Libre AL, Emdadi A, Kansa EJ, Shekarchi M, Rahimian M. A fast adaptive wavelet scheme in RBF collocation for nearly singular potential PDEs. *CMES: Computer Modeling in Engineering & Sciences* 2008; 38: 263-284.

13. Kosec G, Šarler B. H-adaptive local radial basis function collocation meshless method. *CMC: Computers, Materials, & Continua* 2011; 26(3): 227-253.

14. Liu G, Kee B, Lu C. A stabilized least-squares radial point interpolation method (LS-RPCM) for adaptive analysis. *Computer Methods in Applied Mechanics and Engineering* 2006; 195: 4843-4861.

15. Kovačević I, Šarler B. Solution of a phase-field model for dissolution of primary particles in binary aluminum alloys by an r-adaptive mesh-free method. *Materials Science and Engineering* 2005; A413-414: 423-428.

16. Rabczuk T, Belytschko T. A three-dimensional large deformation meshfree method for arbitrary evolving cracks. *Computer Methods in Applied Mechanics and Engineering* 2007; 196: 2777-2799.

17. Ebrahimnejad M, Fallah N, Khoei A. Adaptive refinement in the meshless finite volume method for elasticity problems. *Computers & Mathematics with Applications* 2015; 69(12): 1420-1443.

18. Driscoll TA, Heryudono AR. Adaptive residual subsampling methods for radial basis function interpolation and collocation problems. *Computers & Mathematics with Applications* 2007; 53(6): 927–939. doi: 10.1016/j.camwa.2006.06.005

19. Fornberg B, Zuev J. The Runge phenomenon and spatially variable shape parameters in RBF interpolation. *Computers & Mathematics with Applications* 2007; 54(3): 379–398. doi: 10.1016/j.camwa.2007.01.028

20. Zienkiewicz OC, Taylor RL. *The Finite Element Method: Solid Mechanics*. Butterworth-Heinemann . 2000.

21. Chen Y, Lee JD, Eskandarian A. *Meshless methods in solid mechanics*. New York, NY: Springer . 2006.

22. Mavrič B, Šarler B. Local radial basis function collocation method for linear thermoelasticity in two dimensions. *International Journal of Numerical Methods for Heat and Fluid Flow* 2015; 25: 1488-1510. doi: 10.1108/hff-11-2014-0359

23. Liu G, Gu Y. *An Introduction to Meshfree Methods and Their Programming*. Dordrecht: Springer . 2005.

24. Belytschko T, Lu YY, Gu L. Element-free Galerkin methods. *International journal for numerical methods in engineering* 1994; 37(2): 229–256. doi: 10.1002/nme.1620370205

25. Atluri SN, Zhu T. A new meshless local Petrov-Galerkin (MLPG) approach in computational mechanics. *Computational mechanics* 1998; 22(2): 117–127. doi: 10.1007/s004660050346

26. Oñate E, Perazzo F, Miquel J. A finite point method for elasticity problems. *Computers & Structures* 2001; 79(22-25): 2151–2163. doi: 10.1016/s0045-7949(01)00067-0

27. Pereira K, Bordas S, Tomar S, et al. On the Convergence of Stresses in Fretting Fatigue. *Materials* 2016; 9(8): 639. doi: 10.3390/ma9080639

28. Wei LY. Parallel Poisson disk sampling. *ACM Transactions on Graphics (TOG)* 2008; 27(3): 20. doi: 10.1145/1360612.1360619

29. Schaback R, Wendland H. Characterization and construction of radial basis functions. In: Multivariate Approximation and Applications. Cambridge University Press; 2001: 1–24.

30. Buhmann MD. *Radial basis functions: theory and implementations*. 12. Cambridge university press . 2003.

31. Flyer N, Lehto E. Rotational transport on a sphere: Local node refinement with radial basis functions. *Journal of Computational Physics* 2010; 229(6): 1954–1969. doi: 10.1016/j.jcp.2009.11.016

32. Flyer N, Fornberg B, Bayona V, Barnett GA. On the role of polynomials in RBF-FD approximations: I. Interpolation and accuracy. *Journal of Computational Physics* 2016; 321: 21–38. doi: 10.1016/j.jcp.2016.05.026

33. Franke R. Scattered data interpolation: tests of some methods. *Mathematics of computation* 1982; 38(157): 181–200. doi: 10.1090/s0025-5718-1982-0637296-4

34. Wendland H. *Scattered data approximation*. 17. Cambridge university press . 2004.

35. Afshar M, Naisipour M, Amani J. Node moving adaptive refinement strategy for planar elasticity problems using discrete least squares meshless method. *Finite Elements in Analysis and Design* 2011; 47(12): 1315–1325. doi: 10.1016/j.finel.2011.07.003

36. Sadd MH. *Elasticity: theory, applications, and numerics*. Elsevier/AP. 2nd ed. 2009.

37. Hecht F. New development in FreeFem++. *J. Numer. Math.* 2012; 20(3-4): 251–265. doi: 10.1515/jnum-2012-0013